Spiral Arms in the Asymmetrically Illuminated Disk of MWC 758 and Constraints on Giant Planets

Grady, C.A.; et al., [Unknown]; Thalmann, C.

DOI
10.1088/0004-637X/762/1/48

Publication date
2013

Document Version
Final published version

Published in
Astrophysical Journal

The Astrophysical Journal, 762:48 (13pp), 2013 January 1 doi:10.1088/0004-637X/762/1/48

SPIRAL ARMS IN THE ASYMMETRICALLY ILLUMINATED DISK OF MWC 758 AND CONSTRAINTS ON GIANT PLANETS

C. A. Grady[1,2,3], T. Muto[4], J. Hashimoto[5], M. Fukagawa[6], T. Currie[7,8], B. Biller[10], C. Thalmann[10], M. L. Sitko[11,12,41], R. Russell[13,41], J. Wisniewski[14], R. Dong[15], J. Kwon[5,16], S. Sai[6], J. Hornbeck[17], G. Schneider[18], D. Hines[19], A. Moro Martín[20], M. Feldt[9], Th. Henning[9], J.-U. Pott[9], M. Bonnefoy[9], J. Bouwman[9], S. Lacour[21], A. Mueller[9], A. Juhász[22], A. Crida[23], G. Chauvin[24], S. Andrews[25], D. Wilner[25], A. Kraus[26,42], S. Dahm[27], T. Robitaille[25], H. Jang-Condell[28], L. Abe[29], E. Akiyama[5], W. Brandner[9], T. Brandt[15], J. Carson[30], S. Egner[31], K. B. Follette[18], M. Goto[32], O. Guyon[33], Y. Hayano[31], M. Hayashi[5], S. Hayashi[31], K. Hodapp[33], M. Ishii[31], M. Iye[5], M. Janson[15], R. Kandori[5], G. Knapp[15], T. Kudo[31], N. Kusakabe[5], M. Kuzuhara[5,34], S. Mayama[35], M. McElwain[7], T. Matsuo[5], S. Miyama[36], J.-I. Morino[5], T. Nishimura[31], T.-S. Pyo[31], G. Serabyn[37], H. Suto[5], R. Suzuki[5], M. Takami[38], N. Takato[32], H. Terada[31], D. Tomono[32], E. Turner[14,33], M. Watanabe[39], T. Yamada[40], H. Takami[5], T. Usuda[31], and M. Tamura[5,16]

[1] Eureka Scientific, 2452 Delmer, Suite 100, Oakland CA 96002, USA
[2] ExoPlanets and Stellar Astrophysics Laboratory, Code 667, Goddard Space Flight Center, Greenbelt, MD 20771, USA; carol.a.grady@nasa. gov
[3] Goddard Center for Astrobiology, Goddard Space Flight Center, Greenbelt, MD 20771, USA
[4] Division of Liberal Arts, Kogakuin University, 1-24-2, Nishi-Shinjuku, Shinjuku-ku, Tokyo, 163-8677, Japan
[5] National Astronomical Observatory of Japan, 2-21-1 Osawa, Mitaka, Tokyo 181-8588, Japan
[6] Department of Earth and Space Science, Graduate School of Science, Osaka University, 1-1, Machikaneyama, Toyonaka, Osaka 560-0043, Japan
[7] ExoPlanets and Stellar Astrophysics Laboratory, Code 667, NASA's Goddard Space Flight Center, Greenbelt, MD 20771, USA
[8] University of Toronto, Department of Astronomy and Astrophysics
[9] Max Planck Institute für Astronomie, Königstuhl 17, D-69117 Heidelberg, Germany
[10] Astronomical Institute "Anton Pannekoek," University of Amsterdam, Science Park 904, 1098 XH Amsterdam, The Netherlands
[11] Space Science Institute, 4750 Walnut St., Suite 205, Boulder, CO 80301, USA
[12] Department of Physics, University of Cincinnati, Cincinnati, OH 45221-0011, USA
[13] The Aerospace Corporation, Los Angeles, CA 90009, USA
[14] Homer L. Dodge Department of Physics and Astronomy, The University of Oklahoma, Norman, OK 73019, USA
[15] Department of Astrophysical Sciences, Princeton University, NJ 08544, USA
[16] Department of Astronomical Science, The Graduate University for Advanced Studies (SOKENDAI), 2-21-1 Osawa, Mitaka, Tokyo 181-8588, Japan
[17] Department of Physics and Astronomy, University of Louisville, Louisville, KY 40292, USA
[18] Steward Observatory, The University of Arizona, Tucson, AZ 85721-0065, USA
[19] Space Telescope Science Institute, 3700 San Martin Drive, Baltimore, MD 21218, USA
[20] Departamento de Astrofisica, CAB (INTA-CSIC), Instituto Nacional de Tcnica Aeroespacial, Torrejn de Ardoz, E-28850 Madrid, Spain
[21] LESIA-Observatoire de Paris, CNRS, UPMC Univ. Paris 06, Univ. Paris-Diderot, F-92195, Meudon, France
[22] Leiden Observatory, Leiden University, P.O. Box 9513, NL-2300 RA Leiden, The Netherlands
[23] Laboratoire Lagrange, UMR7293, Université de Nice Sophia-Antipolis, CNRS, Observatoire de la Côte d'Azur, Boulevard de l'Observatoire, F-06304 Nice Cedex 4, France
[24] Laboratoire d'Astrophysique de l'Observatoire de Grenoble, 414, Rue de la Piscine, Domaine Universitaire, BP 53, F-38041 Grenoble Cedex 09, France
[25] Harvard-Smithsonian Center for Astrophysics, 60 Garden Street, Cambridge, MA 02138, USA
[26] Institute for Astronomy, University of Hawaii, 2680 Woodlawn Drive, Honolulu, HI 96822, USA
[27] W. M. Keck Observatory, 65-1120 Mamalahoa Hwy, Kamuela, HI 96743, USA
[28] Department of Physics & Astronomy, University of Wyoming, Laramie, WY 82071, USA
[29] Laboratoire Lagrange, UMR7293, Universit Le de Nice-Sophia Antipolis, CNRS, Observatoire de la Cte d'fAzur, F-06300 Nice, France
[30] Department of Physics & Astronomy, The College of Charleston, Charleston, SC 29424, USA
[31] Subaru Telescope, 650 North A'ohoku Place, Hilo, HI 96720, USA
[32] Universitäts-Sternwarte München Scheinerstr. 1, D-81679 Munich, Germany
[33] The Kavli Institute for the Physics and Mathematics of the Universe, The University of Tokyo, Kashiwa 227-8568, Japan
[34] Institute for Astronomy, 640 N. A'ohoku Place, Hilo, HI 96720, USA
[35] The Graduate University for Advanced Studies (SOKENDAI), Shonan International Village, Hayama-cho, Miura-gun, Kanagawa 240-0193, Japan
[36] Office of the President, Hiroshima University, 1-3-2 Kagamiyama, Higashi-Hiroshima 739-8511, Japan
[37] Jet Propulsion Laboratory, M/S 171-113, 4800 Oak Grove Drive, Pasadena, CA 91109, USA
[38] Institute of Astronomy and Astrophysics, Academia Sinica, P. O. Box 23-141, Taipei 10617, Taiwan, Republic of China
[39] Department of Cosmosciences, Hokkaido University, Sapporo 060-0810, Japan
[40] Astronomical Institute, Tohoku University, Aoba, Sendai 980-8578, Japan
Received 2012 September 13; accepted 2012 October 30; published 2012 December 14

ABSTRACT

We present the first near-IR scattered light detection of the transitional disk associated with the Herbig Ae star MWC 758 using data obtained as part of the Strategic Exploration of Exoplanets and Disks with Subaru, and 1.1 μm *Hubble Space Telescope*/NICMOS data. While submillimeter studies suggested there is a dust-depleted cavity with $r = 0\farcs35$, we find scattered light as close as $0\farcs1$ (20–28 AU) from the star, with no visible cavity at H, K', or K_s. We find two small-scaled spiral structures that asymmetrically shadow the outer disk. We model one of the spirals using spiral density wave theory, and derive a disk aspect ratio of $h \sim 0.18$, indicating a dynamically warm disk. If the spiral pattern is excited by a perturber, we estimate its mass to be 5^{+3}_{-4} M_J, in the range where planet filtration models predict accretion continuing onto the star. Using a combination of non-redundant aperture masking data at L' and angular differential imaging with Locally Optimized Combination of Images at K' and K_s, we exclude stellar or massive brown dwarf companions within 300 mas of the Herbig Ae star, and all but planetary mass companions exterior to $0\farcs5$. We reach 5σ contrasts limiting companions to planetary masses, 3–4 M_J at $1\farcs0$

and 2 M_J at 1.″55, using the COND models. Collectively, these data strengthen the case for MWC 758 already being a young planetary system.

Key words: circumstellar matter – instrumentation: high angular resolution – polarization – protoplanetary disks – stars: individual (MWC 758) – waves

Online-only material: color figures

1. INTRODUCTION

We live in a planetary system with four giant planets, and over the past 15 years a wealth of other massive planets have been identified from radial velocity, transit, and microlensing studies, as well as from direct imaging of nearby stars. These studies have told us a great deal about the frequency of giant planets around older, main-sequence stars, but do not provide insight into when, where, and how frequently they form in their natal circumstellar disks, beyond the trivial constraint that they must have formed while the disks retained abundant gas. A census of signatures of giant planet presence in young disks can be used to bound both the time required to form such bodies, and the portions of the disk occupied by giant planets. Such data are needed to constrain mechanisms for their formation and migration. Interferometric detection of young, Jovian-mass exoplanets and brown dwarfs within their disks is a challenging, but emerging field (Kraus & Ireland 2012; Huélamo et al. 2011), however only a small portion of the disk is sampled. Search techniques focusing on the macroscopic, albeit indirect, signatures that such planets induce in their host disks offer an alternate way of carrying out such a giant planet census.

Recent, high-contrast polarimetric differential imagery of the Herbig F star SAO 206462 has demonstrated one such indirect signature: the presence of spiral arms interpreted as being excited by spiral density waves (Muto et al. 2012). For SAO 206462, two arms were clearly resolved from the disk, and have amplitudes consistent with perturbers that are ∼Saturn-mass objects. SAO 206462 is estimated to have an age of 9 ± 2 Myr (Müller et al. 2011), older than age estimates for the formation of Saturn (Castillo-Rogez et al. 2009) and potentially Jupiter in our solar system. While tantalizing, these data, by themselves, do not provide insight into how common spiral features are in the disks of young stars, or at what point in the evolution of a disk they become detectable.

The Herbig Ae star MWC 758 (HD 36112, A8Ve; $V = 8.27$, $B - V = 0.3$; $H = 6.56$; Beskrovnaya et al. 1999; A5IVe; Meeus et al. 2012) has also been identified as hosting a partially cleared cavity detected in the submillimeter within 0.″2 of the star (Isella et al. 2010; Andrews et al. 2011). The star has been dated to 3.5 ± 2 Myr (Meeus et al. 2012), comparable to the era of giant planet formation in our solar system. The disk still contains molecular and atomic gas (Isella et al. 2010; Salyk et al. 2011; Meeus et al. 2012), while accretion continues onto the star (Beskrovnaya et al. 1999). The revised *Hipparcos* parallax data place the star at 279^{+94}_{-58} pc (van Leeuwen 2007), but much of the literature uses the older *Hipparcos* measurement of 200^{+60}_{-40} pc (van den Ancker et al. 1998). To ensure compatibility with the older literature, we use both distance estimates in this paper. Like SAO 206462, the disk has a low inclination from pole-on ($i = 21 \pm 2°$; Isella et al. 2010), facilitating detection of structure in the inner parts of the system. MWC 758 has a relatively small depletion of millimeter-sized dust grains in the inner portions of its disk (Andrews et al. 2011), and also has not been previously reported to host the distinctive mid-IR dip in the IR spectral energy distribution (SED; Isella et al. 2010). Millimeter interferometry traces gas up to 2.″6 from the star (Chapillon et al. 2008), while millimeter dust emission can be traced ∼1″ from the star. The scale of the disk, the gap size, and the inclination of the outer disk all make this a suitable system to test the hypothesis that SAO 206462 is not unique in hosting spiral arms potentially associated with Jovian-mass planets.

We report the first successful imaging of the disk of MWC 758 in scattered light, the discovery of spiral arms, the detection of a mid-IR dip in the IR SED as well as apparent mid-IR photometric variability, and constrain the mass of companions in and immediately exterior to the disk using a mixture of NIR high-contrast imagery, sparse-aperture masking interferometry at L', and the measured properties of the spiral arms.

2. OBSERVATIONS AND DATA REDUCTION

In this section we discuss observations and data reduction for high-contrast imaging carried out using two instruments at the Subaru Telescope, a reanalysis of *Hubble Space Telescope* (*HST*) coronagraphic imagery, aperture polarimetry and photometry, and assembly of IR SED data, and Very Large Telescope (VLT) sparse aperture masking interferometry. The high-contrast Subaru imagery is processed both for optimal disk detection and for giant planet searches.

2.1. Subaru/HiCIAO Polarimetric Differential Imagery

MWC 758 was observed in the H-band ($\lambda = 1.635^{+0.155}_{-0.145}$ μm) using the high-contrast imaging instrument HiCIAO (Tamura et al. 2006; Hodapp et al. 2008; Suzuki et al. 2010) on the Subaru Telescope on 2011 December 24 UT as part of the Strategic Exploration of Exoplanets and Disks with Subaru (SEEDS) program (Tamura 2009). The AO 188 adaptive optics system (Minowa et al. 2010) provided a stable stellar point-spread function (PSF; FWHM = 0.″07). We observed with a combined angular differential imaging (ADI; Marois et al. 2006) and polarization differential imaging (PDI) mode with a field of view of 10″ by 20″ and pixel scale of 9.5 mas pixel^{-1}. A 0.″3 diameter circular occulting mask was used to suppress the bright stellar halo. Half-wave plates were placed at four angular positions from 0°, 45°, 22.°5, and 67.°5 in sequence with one 30 s exposure per wave plate position for a total of 15 data sets, and a total integration time for the polarized intensity (PI) image of 1440 s, after removing three low-quality images with FWHM > 0.″1, by careful inspections of the stellar PSF. The field rotation in this data set was 9° on the sky, too small for ADI reduction of the data. While a PSF star was observed immediately following the PDI+ADI image set, the PSF had changed significantly from that observed during the observation of MWC 758, precluding conventional PSF subtraction. H-band photometry for MWC 758, taken with the telescope immediately

[41] Visiting Astronomer, NASA Infrared Telescope Facility, operated by the University of Hawaii under contract to NASA.
[42] Hubble Fellow.

before the PDI+ADI data set yielded $H = 6.48 \pm 0.01$ mag in the MKO filter system. The polarimetric data were reduced using the procedure described in Hashimoto et al. (2011) using IRAF.[43]

2.2. Subaru/HiCIAO K_s ADI observations

A second HiCIAO data set was obtained as part of the SEEDS program at K_s ($\lambda = 2.150 \pm 0.160\,\mu$m) on 2011 December 26 UT, with 17 minutes of integration time in ADI mode. The field of view for this data set was $20'' \times 20''$. The data were obtained in direct imaging mode, with no coronagraph, but with short 1.5 s frame times to minimize image saturation. Only the peak of the PSF of MWC 758 was saturated in the K_s data. The 1.5 s integrations were co-added into frames of typically 20 integrations, but after culling, some 10-integration frames were also included. After culling of bad frames, 640 s of integration time were available. The data were processed using variants of Locally Optimized Combination of Images (LOCI) in two ways: using aggressive LOCI (na = 300, nfwhm = 0.5) for a companion search and conservative LOCI (na = 10,000, nfwhm = 1.5) to search for structure in the disk. A discussion of these approaches is in Thalmann et al. (2010). Either LOCI variant suppresses azimuthally symmetric or large angle structure, resulting in voids compared to either the PI data or PSF-subtracted imagery.

2.3. Subaru/IRCS K' Data

MWC 758 and a PSF reference star (HD 242067) were imaged on 2011 November 10 with the Subaru Telescope using the Infrared Camera and Spectrograph (IRCS; Tokunaga et al. 1998) and AO188 in natural guide star mode as part of program S11B-012. The data were obtained in the Mauna Kea K' filter ($\lambda = 2.12\,\mu$m). The native pixel scale is 20.57 mas pixel^{-1}; we used the 0.″15 diameter coronagraphic mask to reduce light from the PSF core spilling out to angular separations of interest for disk detection. Despite variable weather conditions, AO-188 delivered corrected images with a full-width half-maximum of 0.″07.

Our data consist of co-added 15 s exposures taken in ADI mode (Marois et al. 2006) through transit HA = (−0.6, 0.9) with a total field rotation of 127°. Our cumulative integration time for MWC 758 and HD 242067 is 38 minutes and 10 minutes, respectively. Basic image processing follows steps outlined in Currie et al. (2011a, 2011b) for IRCS, including dark subtraction, flat-fielding, and distortion correction (corrected pixel scale = 20.53 mas pixel^{-1}). We considered all HD 202067 frames to construct a reference PSF.

Disk Imaging. To extract a detection of the MWC 758 disk, we explored two approaches: one using PSF subtraction of MWC 758 frames by a median HD 242067 frame and one leveraging upon an "adaptive" LOCI approach (A-LOCI; Currie et al. 2012) for this subtraction. In both cases, we first identified the highest-quality images of MWC 758. Specifically, we monitored the brightness of a background star 2″ from MWC 758 (∼15 mag) and selected only the frames where the star's brightness is within 20% of the peak brightness of any frame. This selection criterion identified 50 MWC 758 frames (750 s total) to focus on for PSF subtraction. Further reduction steps are as follows.

1. *Classical PSF Subtraction.* Here, we subtract the median-combined HD 242067 image from each MWC 758 image. We choose a weighting that minimizes the residuals between separations of 50 pixels and 150 pixels (∼1″–3″), though weightings over slightly different ranges in angular separations (i.e., 0.″75–2.″5) achieve similar results. We also performed a second subtraction weighting the reference PSF by an additional 10% above the value that minimized the residuals for each MWC 758 image. We then derotated and median-combined each PSF-subtracted MWC 758 image.
2. *A-LOCI.* Here, we treat all HD 242067 images separately as a "reference PSF library." Instead of subtracting each reference image from the MWC 758 image at once, we follow the (A)-LOCI approach, subdividing each science image and reference image into annular sections (see Currie et al. 2012; Lafrenière et al. 2007) and determining coefficients for each reference PSF section that minimize the subtraction residuals within that section for a given science image. To better ensure that any "disk" signal is not instead due to PSF mismatch, we compute the cross-correlation function, $r_{\rm corr}$, for each pair of science-reference images and remove poorly correlated image pairs (we find the best results for $r_{\rm corr} > 0.85$). We set the *optimization* area (in units of the image FWHM) over which we define the coefficients to $N_{\rm A} = 3000$ and adopt a radial width for the *subtraction* annulus of $dr = 140$, equal roughly to the angular extent of the disk as seen in the submillimeter (e.g., Andrews et al. 2011).[44]

A-LOCI Limits on Planetary Companions. To search for companions to MWC 758, we employed much more aggressive PSF subtraction settings using A-LOCI on the full set of images (150 images; 37.5 minutes). We adopted A-LOCI settings of $\delta = 0.70$, $N_A = 250$, $dr = 5$, and $r_{\rm corr} = 0.95$ (see Currie et al. 2012; Lafrenière et al. 2007). Additionally, we employed a moving-pixel mask over the subtraction zone, using only the pixels outside of this zone to determine the LOCI coefficients to reconstruct a reference PSF annular region. We then quantify and correct for self-subtraction inherent in A-LOCI by comparing the flux of fake point sources prior to and after processing. We use the measured brightness of the star visible at 2″ ($K' \sim 16.93$) and assume a brightness for MWC 758 of m(K') = 5.804 for flux calibration and thus to determine the planet-to-star contrast.

2.4. Archival HST Coronagraphic Imagery

MWC 758 was observed in the broadband optical twice by *HST*/STIS on 2000 January 16 and January 19 as part of *HST*-GO-8474, with the star placed at a point along the STIS coronagraphic wedge structure (wedgeA1.0) where the wedge occulted the inner 0.″5. The STIS data (observation IDs = O5KQ3010-20 and O5KQ0410-20) were a poor color match to the available library of PSF template data (Grady et al. 2005), yielding disk non-detections with large color mismatch errors. When roll-differenced (Lowrance et al. 2005), a null detection was also seen, indicating either nebulosity that was azimuthally symmetric over 15°, or concentrated within 0.″5 of the star. The STIS data indicate only three point sources in the $25'' \times 50''$ field other than MWC 758, with the nearest at a separation of 2.″1 at PA = 309°.

[43] IRAF is distributed by the National Optical Astronomy Observatory, which is operated by the Association of Universities for Research in Astronomy, Inc., under cooperative agreement with the National Science Foundation.

[44] We detect the inner disk spirals as long as we set dr to be larger than the submillimeter-resolved disk gap ($dr > 25$).

MWC 758 was also observed by *HST*/NICMOS as part of HST-GO-10177 on 2005 January 7. The observations consisted of two independent target acquisitions, short direct images in F171M, the coronagraphic observations at F110W ($\lambda_{cent} = 1.1 \pm 0.3\,\mu$m) with the region at $r \leqslant 0\farcs3$ occulted, and short direct-light F110W imagery with the star unocculted before rolling *HST* by 29.°9 and repeating the sequence. The direct-light imagery yielded F110W magnitudes of 7.314 ± 0.014 mag. The observations obtained at a given spacecraft orientation constitute a "visit." The coronagraphic data for each visit were reduced as described in Schneider et al. (2006), and then a suite of PSF template data from the same *HST* cycle were scaled, registered, and subtracted from the MWC 758 imagery. For the first visit for MWC 758 (visit 31), PSF template data from visits 3D (HD 15745, visit 2), visit 62 and 61(HD 83870), visit 53 (HD 35841 visit 1), visit 41 (HD 22128, visit 1), and 6B (HD 204366, visit 1) provided good color and *HST* residual matches to MWC 758. For the second visit (visit 32), data from visit 48 (HD 38207 visit 1), 4C (HD 30447, visit 1),4D and 4E (HD 72390, visit 1and 2), 42 (HD 22128 visit 2), 62 (HD 83870 visit 2), 65 and 66 (HD 164249, visits 1 and 2), and 6B (HD 204366, visit 1) provided the best matches. The use of independent target acquisitions and largely independent suites of PSF template data mean that medians of the net images for each visit provide two essentially independent observation sets for MWC 758. Both final images provide no indication of nebulosity for $r \geqslant 0\farcs8$, with the bulk of the detected signal within $0\farcs5$ of MWC 758.

The angular scale of the nebulosity is too small compared with the NICMOS F110W resolution element to assess azimuthal symmetry. We have carried out aperture photometry between $0\farcs3 < r < 0\farcs5$ for each of the final net visit images. The total brightness in those annuli in instrumental counts s^{-1} $pixel^{-1}$ are 5183 for visit 31 and 5419 for visit 32, yielding only a $\pm 2\%$ peak to peak difference about a mean of 5301 counts s^{-1} $pixel^{-1}$. Using the NICMOS photometric calibration of 1 counts s^{-1} $pixel^{-1}$ $= 1.26 \times 10^{-6}$ Jy, the total F110W flux density in the measurement annulus is 6.7 mJy. The Two Micron All Sky Survey (2MASS) *J* magnitude for MWC 758 is 7.22 (2.07Jy), so the total 1.1 μm light scattered by this portion of the disk is 0.32%. The nearby point source noted in the 2000 STIS imagery is recovered at $r = 2\farcs215$, PA $= 310.°86$. It is not comoving with MWC 758, and thus is a background object.

2.5. Infrared Survey Facility/Simultaneous IR Polarimeter (SIRPOL) Aperture Polarimetry and Photometry

NIR aperture photometry and polarimetry was carried out for MWC 758 on 2012 March 8 using SIRPOL (Kandori et al. 2006) at the IRSF. The SIRPOL observations were not accompanied by observation of a polarimetric standard star, so the 2MASS system was used to calibrate the NIR magnitudes of MWC 758 using field stars. We measured $J = 7.193$ mag, $H = 6.560$ mag, $Ks = 5.804$ mag with polarizations of 1.63% at *J*, 1.60% at *H* and 0.81% at *Ks*. The polarization levels are typical of low-inclination young stellar objects (Pereyra et al. 2009).

2.6. The IR Spectral Energy Distribution of MWC 758

MWC 758 is a well-studied Herbig Ae star with data from the far-UV through the millimeter. We have assembled a composite SED including *International Ultraviolet Explorer* spectra SWP 53939 and LWP 30023, optical through *M*-band photometry (Malfait et al. 1998; Bogaert 1994; de Winter et al. 2001; Beskrovnaya et al. 1999), 2MASS, *Midcourse Space Experiment*, *IRAS*, and *Infrared Space Observatory* SWS data, two epochs of Broadband Array Spectrograph System spectrophotometry (Hackwell et al. 1990), *Spitzer* IRS data originally published by Juhász et al. (2010), *AKARI*, and the *Wide-field Infrared Survey* data (excepting band 2, 4.5 μm). We also include the *HST*/NICMOS F110W photometry as well as the photometry obtained in tandem with the HiCIAO PDI observation and the SIRPOL data. The data, color-coded by source, are shown in Figure 1, together with a Kurucz $T = 8250$ K photospheric model, reddened by an $R = 3.1$ extinction curve with $E(B - V) = 0.13$. A similarly good fit at short wavelengths can be achieved without foreground reddening and with $T_{\rm eff} = 7580$ K, as used by Andrews et al. (2011). This model requires a contribution from UV excess emission (e.g., accretion luminosity) to match the observed FUV flux (Martin-Zaïdi et al. 2008), but is consistent with low line-of-sight extinction ($E(B - V) \leqslant 0.1$) for the source to be detected by FUSE.

2.7. VLT/NACO Sparse Aperture Masking Interferometry

MWC 758 was observed on 2012 March 11 with VLT/NACO Sparse-Aperture Masking[45]. Observations were taken in the L' band ($\lambda_{L'} = 3.80 \pm 0.31\,\mu$m) using the "7 holes" aperture mask and the IR wavefront sensor (WFS). A total of 24 data cubes, each one made of 330 frames of 0.12 s integration time were obtained for MWC 758 in L' on the night of 2012-03-12(UT). Observations of two calibrator stars, HR 1921 and HD 246369, were obtained for a total of eight data cubes, interleaved every eight MWC 758 data cubes. The MWC 758 observations were processed with the Observatoire de Paris SAMP pipelines (Lacour et al. 2011a, 2011b).

The use of the "7 holes" (C7-892, Tuthill et al. 2010) aperture mask transforms the telescope into a Fizeau interferometer. The point spread function is a complex superposition of fringes at given spatial frequencies. In specific cases, pupil-masking can outperform more traditional differential imaging for a number of reasons (Tuthill et al. 2006; Lacour et al. 2011b). First, the masks are designed to have non-redundant array configurations that permit phase deconvolution; slowly moving optical aberrations not corrected by the AO can be accurately calibrated. Second, the mask primarily rejects baselines with low spatial frequency and passes proportionately far more baselines with higher λ/B (where B is baseline length) resolution than does an orthodox fully filled pupil. Third, high-fidelity recovery of phase information allows "super resolution," with a marginal loss of dynamic range up to $\lambda/2D$ (where *D* is the mirror diameter). The principal drawback is a loss in throughput so that photon and detector noise can affect the signal-to-noise ratio even where targets are reasonably bright for the AO system. The effective field-of-view of sparse aperture masking (SAM) is determined by the shortest baseline so that the technique is not competitive at separations that are greater than several times the formal diffraction limit. For more details on the SAM mode, see, e.g., Lacour et al. 2011a; Tuthill et al. 2010.

3. RESULTS

In this section we discuss the disk detection, compare it with synthetic imagery for a model fitting the submillimeter continuum data and the IR SED, report the discovery of spiral

[45] Program ID: 088.C-0691(A).

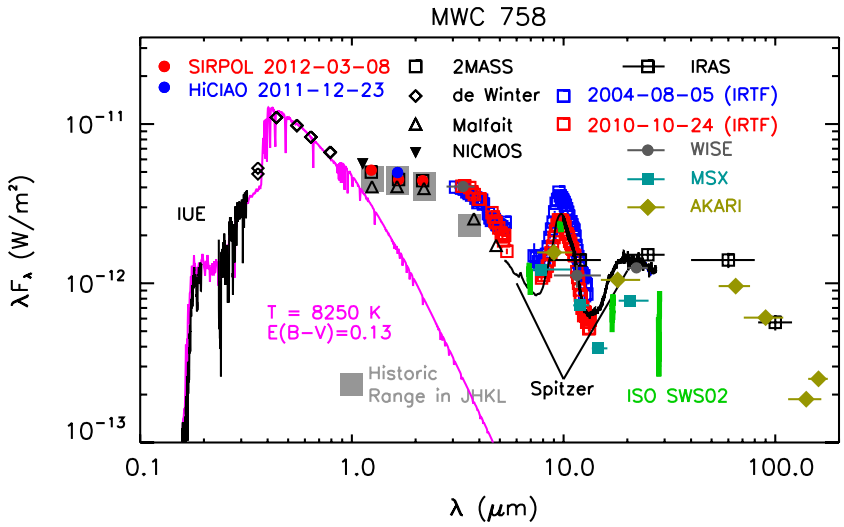

Figure 1. Composite SED of MWC 758. The star has limited UV data, optical data indicating minor photometric variability, consistent with a low inclination, NIR data showing a larger range, and mid-IR data from a variety of sources indicating a factor of 2–3 flux variation from 5 to 30 μm. The mid-IR data, particularly the Spitzer IRS spectrum previously presented by Juhász et al. (2010), clearly demonstrate the dip in the SED characteristic of pre-transitional, or gapped disks.

arms in the disk, and following Muto et al. (2012) discuss the implications for a giant planet capable of exciting the more completely imaged spiral arm. We next discuss limits on stellar, brown dwarf, and giant planetary mass companions provided by the sparse aperture masking data and the Subaru observations.

3.1. MWC 758 as a Gapped Disk

Previous studies of MWC 758 had identified this system as hosting a cavity visible in submillimeter continuum interferometry, but lacking a very conspicuous dip in the IR SED near 10 μm (Isella et al. 2010; Andrews et al. 2011). In contrast, our composite SED based on an assembly of archival photometry and spectrophotometry clearly shows a dip (Figure 1), with indications of mid-IR variability, providing the first independent confirmation that MWC 758 is what has been termed a gapped or "pre-transitional" disk with an inner disk structure (Isella et al. 2008), a wide gap, and an outer disk seen in millimeter data (Isella et al. 2010), and thermal emission (Mariñas et al. 2011). When compared with other transitional disks, the depth of the 10 μm dip is smaller, consistent with the lack of a cavity in our F110W, H, K', and K_s imagery. Modeling of other disks with HiCIAO observations have suggested that the absence of a cavity at H is not atypical of transitional disks, and can be accounted for by grain filtration (Rice et al. 2006), with large mm-sized grains deeply depleted in the cavity region, while smaller grains, which are more tightly coupled to the gas, are less depleted (Dong et al. 2012; Zhu et al. 2012).

3.2. The Structured Disk of MWC 758

The disk of MWC 758 is detected in polarized, scattered light from 0.″2 to 0.″8 (223 AU assuming $d = 279$ pc or 160 AU assuming $d = 200$ pc) in polarized intensity at H-band (Figure 2). The disk detection did not require unusually favorable conditions (e.g., MWC 480; Kusakabe et al. 2012): H-band photometry was in the range of previous NIR data for the star (Figure 1). The detected nebulosity is highly asymmetric about the star, with the greatest extent seen to the west of the star at H, while to the east, nebulosity is not detected exterior to 0.″5. To the west of the star, the scattered light disk extends as far as the submillimeter continuum can be traced (Isella et al. 2010; Figures 2(a) and (b)). The disk is also detected at K_s (Figure 2(c)) to within 0.″1 of the star, and in K' (Figure 2(d)) to within 0.″25, and at 1.1 μm (Figure 2(e)). A false-color composite of the H PI (blue) and K' (red) is shown in Figure 2(f). This composite image also allows us to identify a region of reduced polarization intensity along PA $= 155° \pm 5°$ and PA $= 330° \pm 5°$, aligned with the projection of the disk semiminor axis. To the east of the star, the H PI surface brightness $\propto R^{-5.7\pm0.1}$ (Figure 3). To the west of the star, it drops as $\propto R^{-2.8\pm0.1}$, consistent with the disk exhibiting some flaring.

Unlike other protoplanetary (Kusakabe et al. 2012) or transitional disks (Muto et al. 2012) imaged with HiCIAO in H PI, the reflection nebulosity is not aligned with the disk semimajor axis (PA $= 65 \pm 7°$). Moreover, we detect scattered light within the region of partial clearing reported in the submillimeter continuum (Isella et al. 2010), rather than the expected cavity. The PI for $r \geqslant 0.''2$ is 6.095 ± 0.085 mJy, or 0.09% relative to the star. Between 0.″3 and 0.″5 the PI is 2.72 mJy, or 0.0425% relative to the star, indicating that the region of the arms is providing half of the observed polarized intensity. If we assume neutral scattering, the PI in the arm region $0.''3 \leqslant r \leqslant 0.''5$ can be compared with the F110W total intensity of 0.32%, indicating a polarized light fraction of ∼13.3% which is in the range of polarization fractions observed for other Herbig Ae stars.

3.3. Comparison with Monte Carlo Radiative Transfer Models for the Disk

Given the structure seen in the H-band PI imagery, it is natural to explore what we would have expected to have seen based on combined modeling of the submillimeter data and the IR SED. To address this goal, we carried out Monte Carlo radiative transfer modeling using the code developed by Whitney et al. (2003a, 2003b; B. A. Whitney et al. 2013, in preparation), with modifications as described in Dong et al. (2012). In particular, we adopt a disk outer radius of 200 AU, viewed at $i = 23°$, and assume an accretion rate of $\dot{M} = 10^{-8}\ M_\odot\ \mathrm{yr}^{-1}$ (Andrews et al. 2011). We model the entire disk with two components: a thick disk with small grains (∼μm-sized and smaller), which represents the pristine dust grains from the star forming environment, and a thin disk with large grains (up to ∼mm-sized), which is the result of dust growth and settling

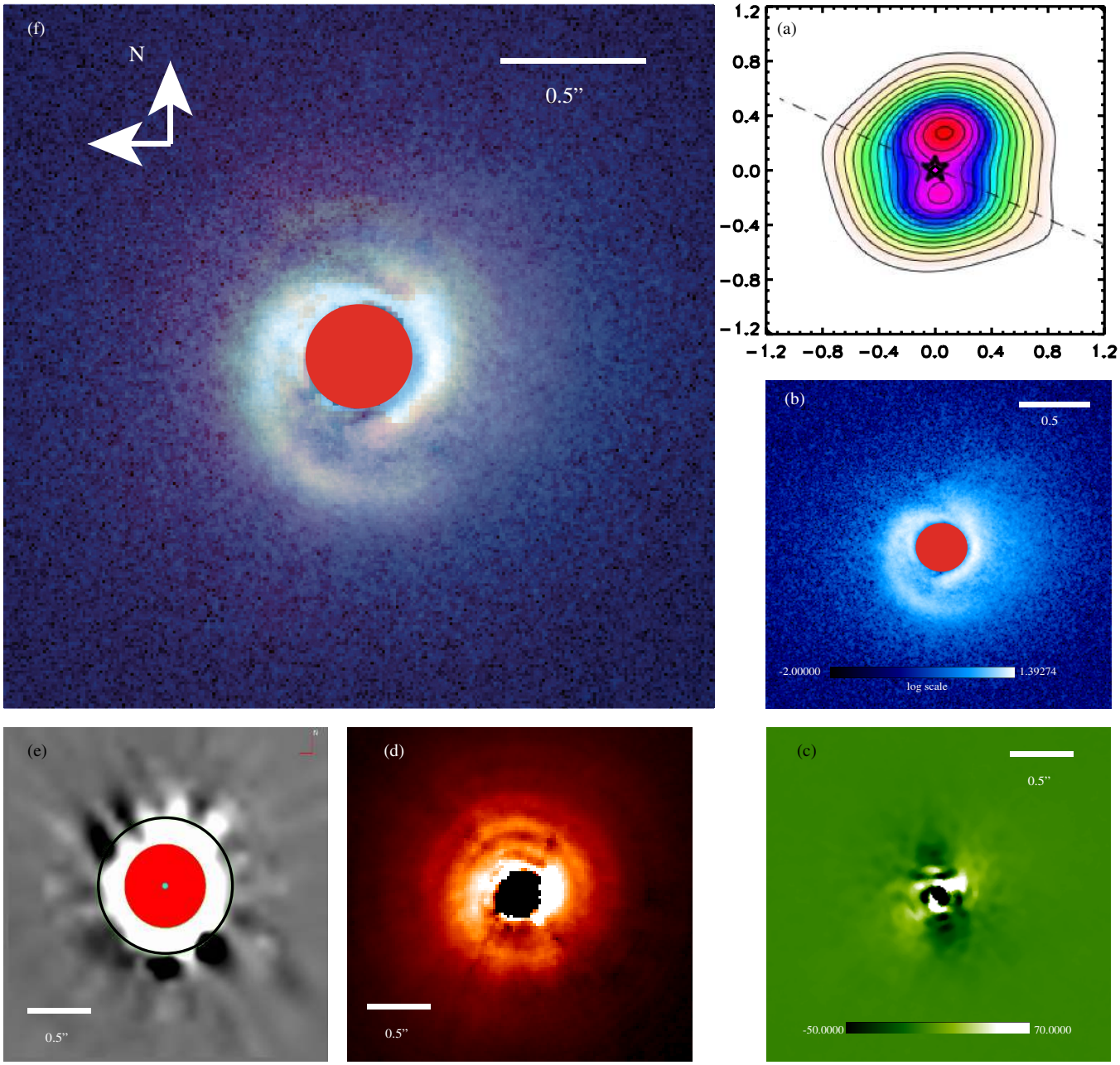

Figure 2. Disk of MWC 758: (a) the 880 μm continuum after Isella et al. (2010), the dashed line indicates the disk semimajor axis, (b) *H*-band polarized intensity, (c) K_s data with conservative LOCI processing, (d) K' intensity with conservative LOCI processing, (e) *HST*/NICMOS total intensity data following PSF subtraction, (f) color composite of H PI and K' data. The images are all 2.″4 on a side, and oriented with north up and east to the left. The HiCIAO H PI data use a 0.″3 diameter coronagraphic spot, the NICMOS data uses a 0.″6 spot. The IRCS data use an 0.″15 diameter occulting spot, and the K_s data have an inner working angle of 0.″1.

toward the disk mid plane. We adopt the interstellar medium dust model in Kim et al. (1994) for our small-grain dust, and the dust model 2 from Wood et al. (2002) for our large-grain dust, which has a power law size distribution up to 1 mm (with power law index 3.5). The large-to-small-dust mass ratio is assumed to be 0.85/0.15 as in Dong et al. (2012). The properties of the grains can be found in Wood et al. (2002).

With these assumptions, the total dust mass of the disk is 0.067 M_J. The radial surface density distribution of both dust grain populations is assumed to have the following profile

$$\Sigma(R) = \Sigma_0 \left(\frac{1\ \mathrm{AU}}{R}\right)^{\alpha}, \quad (1)$$

where Σ_0 is the normalization factor, R is radius, and α is the power law index. In the vertical direction, we assume

$$\rho(R, z) = \frac{\Sigma(R)}{\sqrt{2\pi}H} e^{-z^2/2H^2}, \quad (2)$$

where $\rho(R, z)$ is the local volume density, z is the vertical dimension, and H is the scale height (input parameters in the code). Radially, both scale heights for the small and large dust vary with radius as

$$H \propto R^{\beta}, \quad (3)$$

where β is a constant power law index, assumed to be 1.08 in this work. The scale height, h, of the small dust is assumed to be 15 AU at 100 AU, while that for the large dust is assumed to be

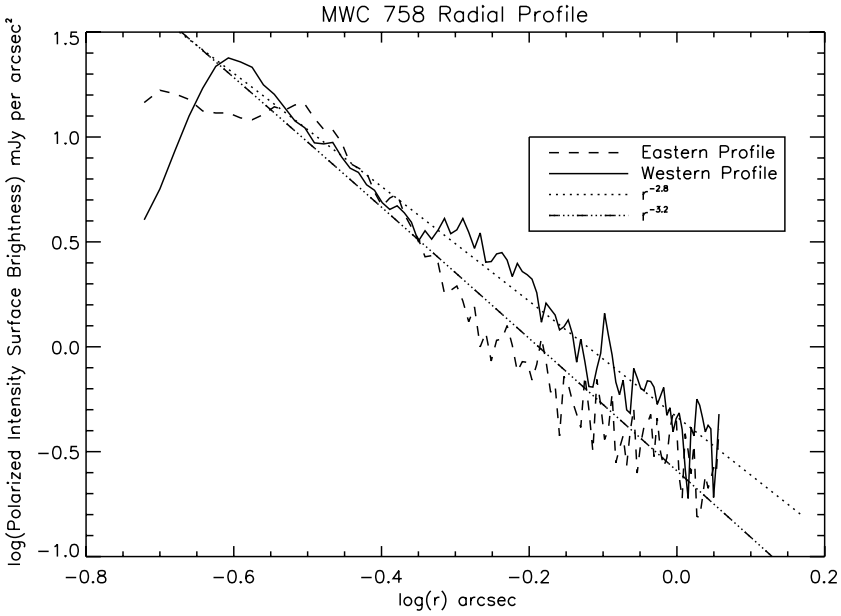

Figure 3. Radial surface brightness profiles at PA = 270° (black) and PA = 90° (gray) together with power-law fits.

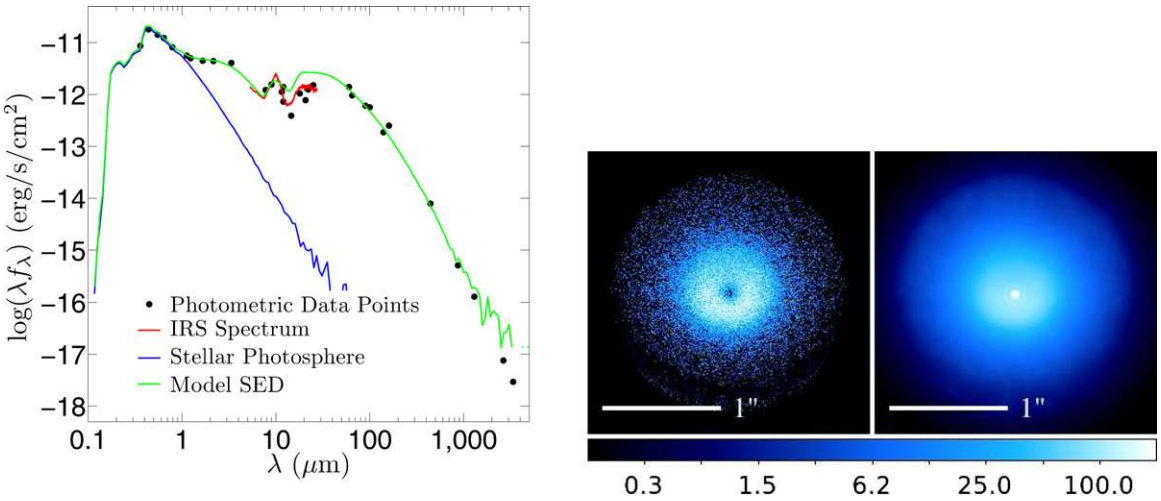

Figure 4. Radiative transfer modeling results for MWC 758, showing the SED (left), the raw model *H*-band polarized light image (middle) with a cavity visible in the inner disk, and the convolved *H*-band polarized light image (right). The images are in unit of mJy arcsec^{-2}.

(A color version of this figure is available in the online journal.)

1/5 of the h for the small dust, to reflect the fact that big grains tend to settle to the disk mid-plane, while small grains tend to be well coupled with the gas and have a much larger vertical extension (Dullemond & Dominik 2004, 2005; D'Alessio et al. 2006).

Our disk model has a gap structure located from 0.5 AU to 73 AU. Inside the gap there are no large dust grains, as suggested by the spatially resolved submillimeter array observations, which revealed a clear cavity 73 AU in radius at 880 μm (Andrews et al. 2011). However, the *H*-band PI data demonstrate that there is a significant amount of scattered light within this radius, indicating the presence of starlight-scattering small dust grains. We set $\alpha = 1$ for both dust populations in the outer disk, and $\alpha = -3$ for the small dust inside the gap, with a continuous surface density distribution across the gap edge. As discussed in detail in Dong et al. (2012), this kind of surface density distribution of the small dust results in a heavy depletion at the inner disk, producing the IR excess depression around 10 μm on the SED seen in transitional disks, but a smooth NIR scattered light image with no breaks or discontinuities of the surface brightness radial profile at the inner edge of the outer disk. MWC 758 has an NIR excess (Figure 1), and VLTI/AMBER data (Isella et al. 2008) indicating a small amount of hot, small dust grains at the innermost radii. To reproduce these features, we put a inner rim located at 0.33–0.5 AU. The surface density of the rim is ~0.002 g cm^{-2}.

Figure 4 shows the model SED and *H*-band polarized light image from the modeling, with the disk major axis horizontal, and the near side of the disk in the bottom half of the image. The model images show both the PI as modeled, and after convolution with an observed HiCIAO PSF (see Dong et al. 2012 for details). The model reproduces the extent of the polarized intensity to the west of the star, but, as expected, predicts a similar extent of the scattered-light disk to the east of the star, beyond 0.″5. The model predicts a bright arc on the near-side of the image, which is not seen in the data. The raw model

imagery predicts a cavity visible at H in the immediate vicinity of the star, which is not conspicuous after convolution with the PSF, and which is in the region occulted by the coronagraph in our *H*-band data. Higher Strehl ratio and smaller inner working angle imagery, such as can be provided by extreme AO systems, will be required to test these predictions of the model.

3.4. Spiral Arms

The most distinctive features in the NIR images that are not captured in the model imagery are a spiral feature on the east side of the star, wrapping toward the south, which we term the southeast (SE) arm, and a similar feature originating in the NW and wrapping to the north, which we term the northwest (NW) arm. The spiral arms are most clearly detected interior to 0.″5 (100 AU for $d = 200$ pc, or 140 AU for $d = 279$ pc). Our data for MWC 758 therefore demonstrate that SAO 206462 (Muto et al. 2012) is not unique in hosting spiral arms straddling the region of the partially cleared millimeter cavity. Moreover, like SAO 206462, and unlike HD 142527 (Casassus et al. 2012; Rameau et al. 2012) there is no indication of a cleared zone at *H*-band for $r \geqslant 0.''2$ (40 AU for $d = 200$ pc, 56 AU for $d = 279$ AU).

The spiral arms in the disk of MWC 758 are detected as a contrast in surface brightness. The drop in polarized surface brightness immediately exterior to the SE arm is consistent with that arm fully shadowing the outer disk. Shadowing by the NW arm is less complete: Some signal is seen beyond the arm in our 2011 data. We measure the SB contrast of the arm features by measuring the amplitude at the SE arm at PA $= 90^\circ$ and the corresponding surface brightness the same distance from the star at PA $= 270^\circ$. For the SE arm we find a ratio of 50% $\pm$ 20%. The angular extent of the NW arm is sufficiently small that to confidently measure the amplitude and fit the pattern we will require data obtained with a combination of higher Strehl ratio, and a coronagraph with smaller inner working angle, such as may be provided by SCExAO in tandem with AO188+HiCIAO on Subaru (Martinache et al. 2011, 2012). We therefore restrict all but qualitative discussion of the arms to the SE arm.

Both of the arms have the same rotation sense. If they are trailing structures, as expected for spiral density waves, the rotation of the disk, and any companions associated with the arms, is clockwise. Comparison with the millimeter data (Isella et al. 2010), then indicates that the northwest side of the disk is the near side of the disk. Our PI image is fully consistent with the disk being viewed at a low inclination from face-on, since it lacks the compression of the PI toward the disk semimajor axis, which is conspicuous at $i \geqslant 38^\circ$ (Kusakabe et al. 2012). Given the asymmetric illumination of the disk, we adopt the millimeter disk inclination $i = 21 \pm 2^\circ$ (Isella et al. 2010).

3.5. The Disk at Other Wavelengths

To be correctly interpreted as spiral density waves, the spiral arms should be recovered in observations made at different wavelengths and with different instruments. The IRCS K' data detect the disk in scattered light to at least 0.″5 from the star, and recover both spiral arms using either classical PSF subtraction and using A-LOCI as long as we set dr to be larger than the size of the disk gap ($dr > 25$). The K_s data sample the disk less completely, due to the very short integration times for each individual exposure. However, they recover the inner portions of the arms, in the conservative LOCI processing of the data, to an inner working angle of 0.″1 but suppress them in aggressive LOCI processing.

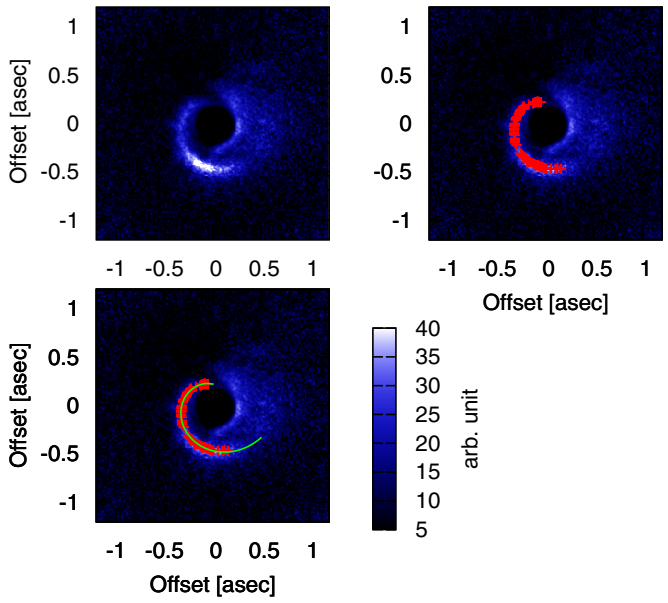

Figure 5. Top left: the surface brightness of the scattered light normalized by r^2, where r is the distance from the central star. The shape of the spiral is more enhanced, and this data is used for the analysis for the spiral fitting. Top right: the points that represent the spiral shape are shown by red points, which are used as data points for the fitting. Bottom left: the shape of the spiral given by Equation (4) with the best-fit parameters (Table 1) is shown by green curves. The red points are the same with those in the top right panel.

(A color version of this figure is available in the online journal.)

The brightest portion of the disk as seen at 1.1 μm is the region occupied by the spiral arms, between 0.″3 and 0.″5. The *HST*/NICMOS data from 2005 provide no indication of the asymmetric illumination seen in the 2011 data: This may either be due to changes in illumination over time, or to contrast limits of the *HST*/NICMOS data. However, we note that asymmetric illumination of the disk was not seen in the *HST*/STIS data from 2000. Additional observations will be required to establish whether the illumination of the outer disk changes with time. The locations of the arms coincide with the brightest 12 μm signal from the MWC 758 disk (Mariñas et al. 2011). The coincidence of structural features in scattered light, polarized scattered light, and in thermal emission indicate that the spiral arms are density features, and not merely distortions of the disk surface. The rapid drop in surface brightness seen in the *H*-band PI data to the east of the spiral arms (Figure 3) further indicates that the arm is optically thick and extends sufficiently far above the undistorted disk surface to cast a long shadow. The region of the NW arm near PA $= 340^\circ$ coincides with the clump in continuum emission noted by Isella et al. (2010), although with a synthesized beam size of 0.″76 $\times$ 0.″56, the available submillimeter continuum interferometry lacks the angular resolution to directly detect the arms. As the angular resolution of submillimeter interferometry improves, we expect that these features should be detectable in continuum and gas observations, such as can be provided once ALMA reaches its full extent.

3.6. Fitting the Spiral Arms

We follow the approach given in Muto et al. (2012) to fit the spiral arms. Our initial fits have been restricted to the *H*-band PI data. Given the nearly face-on system inclination, we have not de-projected the data to compensate for the non-zero inclination, but have compensated for the r^{-2} drop in illumination of the disk (Figure 5). From the data, we have looked for the local maxima

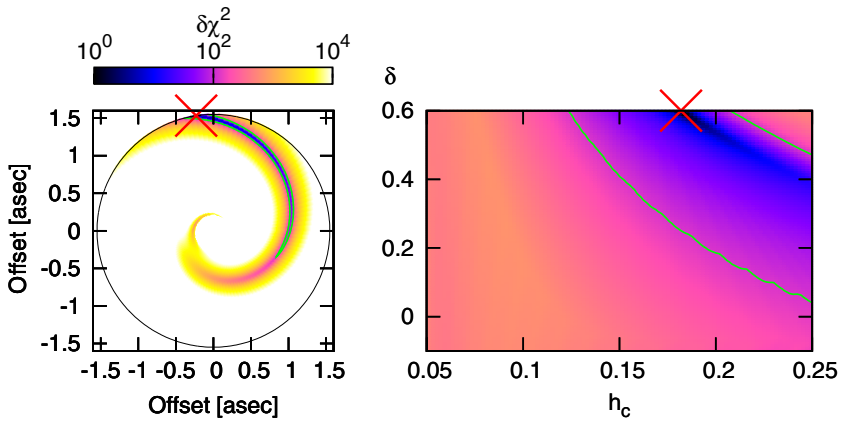

Figure 6. Left: the degeneracy of (r_c, θ_0) parameters plotted in the 2D spherical coordinate. The color shows the values of $\delta\chi^2$ with respect to the best-fit values, which are shown by the red cross. The contour of 99% confidence level is shown by the green line, and the black circle is the radius of $r = 1\farcs55$, which is the upper limit of the parameters that are searched. Right: the degeneracy of (h_c, δ) parameters. As in the left panel, the contour of 99% confidence level is shown by green curves and the best-fit parameter is indicated by the red cross.

(A color version of this figure is available in the online journal.)

of the surface brightness $\times r^2$ profile for each radial profile both for the SE spiral and the NW spiral. If the features are a part of a ring, the points would lie horizontally in a polar coordinate plot of the intensity. The SE spiral is clearly non-axisymmetric, but only a small angular extent of the NW arm is non-axisymmetric, given the inner working angle of our data. For the remainder of this study we restrict our attention to the SE spiral.

Assuming $i = 21^\circ$ and PA $= 65^\circ$ for the disk major axis, the fitting function for the spiral is

$$\theta(r) = \theta_0 + \frac{\mathrm{sgn}(r - r_c)}{h_c} \times \left[\left(\frac{r}{r_c}\right)^{1+\delta} \left\{ \frac{1}{1+\delta} - \frac{1}{1-\gamma+\delta} \left(\frac{r}{r_c}\right)^{-\gamma} \right\} - \left(\frac{1}{1+\delta} - \frac{1}{1-\gamma+\delta} \right) \right]. \quad (4)$$

Here, as in SAO 206462 paper, The corotation point (∼launching point of the spiral) is at (r_c, θ_0). The disk rotation profile is $\Omega(r) \propto r^{-\gamma}$ and the disk sound speed profile is $c(r) \propto r^{-\delta}$. The disk aspect ratio (H/R) at the corotation radius is h_c. Note that assuming $H = c/\Omega$, β that appears in Equation (3) is related to γ and δ by $\beta = \gamma - \delta$. We also note that if the disk temperature varies as $T \propto r^{-q}$, q and δ are related by $\delta = q/2$ since temperature is proportional to the square of the sound speed and the disk sound speed profile is $c(r) \propto r^{-\delta}$.

Note that the sign after the first θ_0 in the right hand side of Equation (4) is different from that in Muto et al. (2012), due to the counter clockwise rotation of the SAO 206462 disk.

There are five fitting parameters: $(r_c, \theta_0, h_c, \gamma, \delta)$. Among them, three (h_c, γ, δ) are determined by the disk structure and the two (r_c, θ_0) determine the location of the spiral feature. Assuming Keplerian rotation, $\gamma = 1.5$. In our study of SAO 206462 (Muto et al. 2012), the sound speed profile δ was fixed, but we have varied this parameter as well. There is a range of values related to δ in the literature, ranging between 0.45 (the ψ parameter in Andrews et al. 2011), 0.19 (q in Chapillon et al. 2008), and 0.05 (the ζ parameter in Isella et al. 2010). We note that for $\delta = 0.5$, the opening angle of the disk is almost constant, in disagreement with our radial SB profile. We looked for the best-fit parameters in the least χ^2 sense by dividing the (r_c, θ_0) space in 128×128 cells and (h_c, δ) space in 100×100 cells with equal spacing in the linear scale. The parameter space explored, and best-fit parameters, are shown in Table 1. Our value for h_c is similar to that derived by Andrews et al. (2011). The external perturber fit resulted in a reduced χ^2 of 0.68.

Table 1
Spiral Arm Fitting

Parameter	Search Range	Best-fit External Perturber
r_c	$0\farcs05 \leqslant r_c \leqslant 1\farcs55$	$r_c = 1\farcs55$
θ	$0 \leqslant \theta_0 \leqslant 2\pi$	$\theta_0 = 1.72$[rad] [a]
h_c	$0.05 \leqslant h_c \leqslant 0.25$	$h_c = 0.182$
δ	$-0.1 \leqslant \delta \leqslant 0.6$	$\delta = 0.6$

Note. [a] Measured from PA $= 90^\circ$.

Now we consider the degeneracy of the parameter space. The degeneracy of parameters of the spiral position (r_c, θ_0) and those of the disk parameter (h_c, δ) are investigated separately. The left panel of Figure 6 shows the degeneracy of (r_c, θ_0). The best fit to the SE spiral arm places the launching point of the spiral outside of both where we detect the spiral arm, and at a radius exterior to the dust disk as seen in the submillimeter. It might worth pointing out that there is a range of parameters where the corotation radius r_c is inside the spiral arms and where the values of $\delta\chi^2$ becomes small, although these parameters are outside the range of 99% confidence.

In the right panel of Figure 6, we show the degeneracy in the (h_c, δ) parameter space. For each fixed values of (h_c, δ), we looked for the set of (r_c, θ_0), which gives the minimum $\delta\chi^2$ value. Note that $\delta = 0$ is a constant temperature, flared disk and $\delta = 0.5$ is the constant opening angle disk. Although the degeneracy is significant, we favor a disk with a rather flat, constant opening angle geometry. In this case, the spiral can cast a long shadow over the outer disk rather easily, if the spiral has sufficient amplitude, as is observed in the H-band PI imagery. We also note that the parameters for a warmer disk ($h_c \geqslant 0.1$) are favored.

3.7. Estimating the Perturber Mass for the SE Spiral

If we assume that a perturbing body excites the spiral arm, the mass of the perturber launching the spiral density waves can

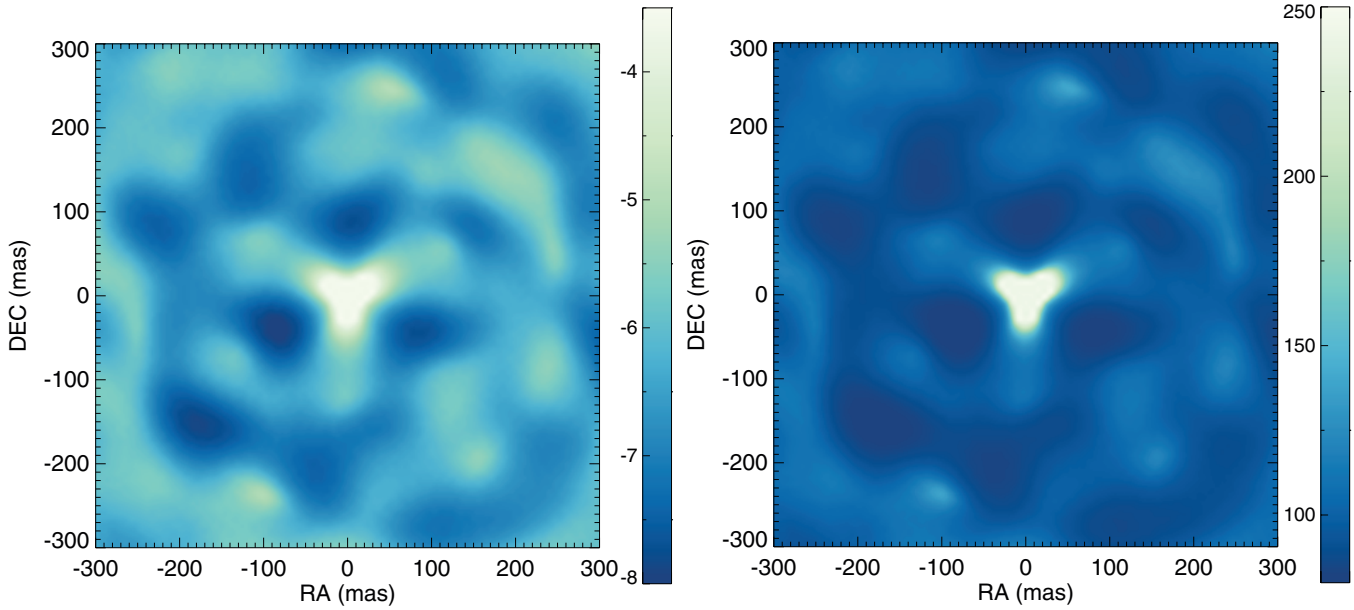

Figure 7. Left: 5σ contrast map from our SAM NACO observations. Our observations are sensitive to companions 4–8 mag fainter than the primary star at separation of 300 mas or less. Right: minimum detectable companion mass map. Contrasts were converted to minimum detectable companion mass using the models of Baraffe et al. (1998, 2002), and adopting an age of 3.7 Myr and a distance of 279 pc. We are sensitive to companions right down to the star/brown dwarf boundary, i.e., $\sim$80 $M_{\rm Jup}$. From these observations, we conclude that MWC 758 does not have a low-mass stellar companion within 300 mas of the primary star.

(A color version of this figure is available in the online journal.)

be estimated independent of knowledge of where it might be located, if there are data indicating the relative disk scale height (h_c), the mass of the star, and the amplitude of the spiral pattern as follows:

$$M_p/M_* = (\text{Pattern Amplitude})\,(h_c)^3.$$

Adopting $1.8 \pm 0.2\,M_\odot$ for the stellar mass, $h_c = 0.18$ from the pattern fitting for the SE spiral, and a pattern amplitude of 0.5 ± 0.2 from the surface brightness contrast for the SE arm, we find a perturber mass for the SE pattern of $\sim 5^{+3}_{-4}\,M_J$, consistent with the perturber being a giant planet, but excluding stellar or brown dwarf mass objects. This mass estimate is also consistent with accretion continuing onto the star.

3.8. Contrast Limits on Companions to MWC 758 Within or Near the Disk

The 5σ contrast map from our SAM NACO observations is presented in Figure 7(a). At L' band, SAM is sensitive to companions at separations $\leqslant$300 mas from the primary. Attained contrasts range from $\Delta\text{mag}(L) = -4$ to $\Delta\text{mag}(L) = -8$. Contrasts were converted to minimum detectable companion mass using the models of Baraffe et al. (1998, 2002), and adopting an age of 3.7 Myr and a distance of 279 pc. Similar limits are achieved for 5 Myr and a distance of 200 pc. With these assumptions, minimum detectable mass images are shown in Figure 7(b). Our SAM observations are sensitive down to very low mass stellar companions ($\sim$80 M_J): we conclude that MWC 758 is a single star. Thus, our limits for companions within the region occulted in the HiCIAO H-band PI data are at the low end of the stellar/high end of the brown dwarf range.

Figure 8(a) shows S/N maps for the K_s and K' data sets. Within 3″ of the star, the only point-source object is the $K = 16.98$ mag background star, which was detected at 37σ at K_s. K-band 5σ contrast limits for the K_s data (from 0.″1–0.″25) and the K' data ($r \geqslant 0.''25$) are shown in Figure 9. The deepest imagery in our set of observations is the IRCS K' data which provide 5σ contrasts of 1.4×10^{-4} at 0.″25, 2.1×10^{-5} at 0.″5, 3.3×10^{-6} at 1″, and 1.12×10^{-6} at 1.″55 (see Figure 8).

Adopting an age of 5 Myr and the COND models (Baraffe et al. 2003), these contrasts correspond to 5 σ detection limits of 15–20 M_J at 0.″25, 8–10 M_J at 0.″5, and 3–4 M_J at 1″, and near 2 M_J at 1.″55 for distances of 200 and 279 pc respectively. These data exclude brown dwarf-mass companions exterior to 0.″5 and are in general agreement with the mass estimates based on the spiral arm fitting. Interior to 0.″5, our upper limits are consistent with at most low-mass brown dwarf close companions to MWC 758. Our mass limits are consistent with accretion continuing onto the star, as observed, and as predicted for disks with Jovian-mass companions (Rice et al. 2006; Lubow & D'Angelo 2006).

4. DISCUSSION

Confirmation that MWC 758 is a gapped disk. Historically, transitional disks have been defined by the weakness of the IR SED near 10 μm, compared with the excess at longer wavelengths (and in some systems at shorter wavelengths), in addition to the detection of a wide gap or cleared cavity in submillimeter continuum aperture synthesis imagery. Figure 1 demonstrates the presence of a dip in the IR SED near 10 μm. Together with VLTI data indicating an inner dust belt (Isella et al. 2008), and the central cavity and outer disk seen in millimeter interferometry (Isella et al. 2010), and thermal emission (Mariñas et al. 2011), the SED data indicate that MWC 758 is a transitional disk. When compared with other transitional disks, the depth of the 10 μm dip is smaller, consistent with less complete clearing of the few to 100 AU region. However, the depletion of millimeter-sized grains (Andrews et al. 2011) is similar to SAO 206462.

Spiral arms are not unique to SAO 206462. MWC 758 is the third Herbig Ae star to show spiral arms in the inner parts of the disk, extending from the region of the submillimeter cavity (Isella et al. 2010) into the outer disk. Like SAO 206462

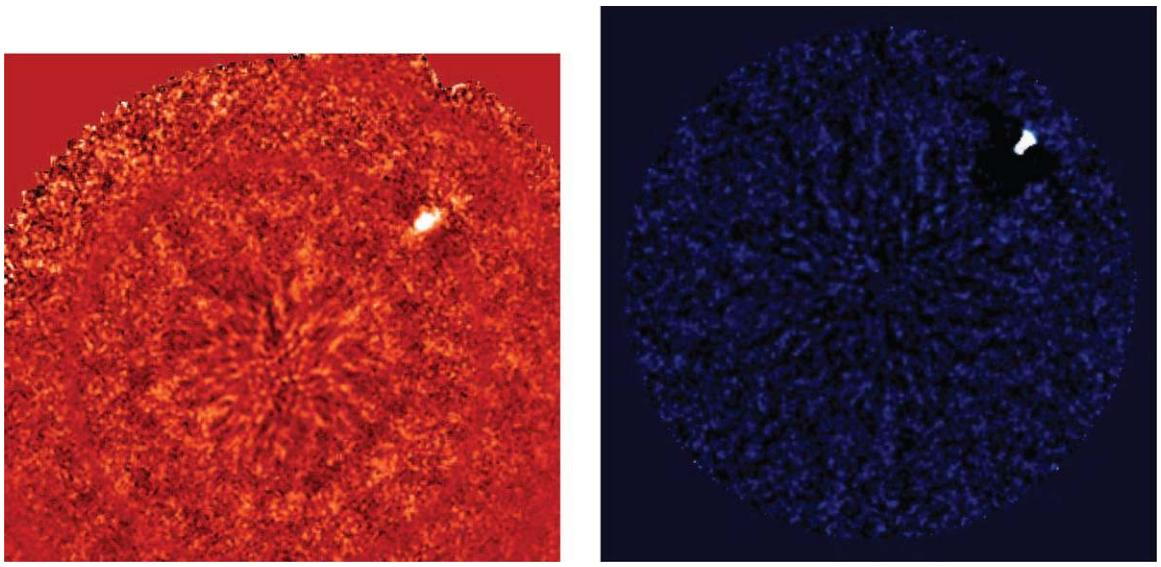

Figure 8. Aggressive LOCI S/N map for MWC 758 at K_s (left) and K' (right). The field shown for the K_s data is ~2.″5, while that for the K' data has an outer radius of 3.″04. The only point source detected in either data set is the background object first seen by *HST*.

(A color version of this figure is available in the online journal.)

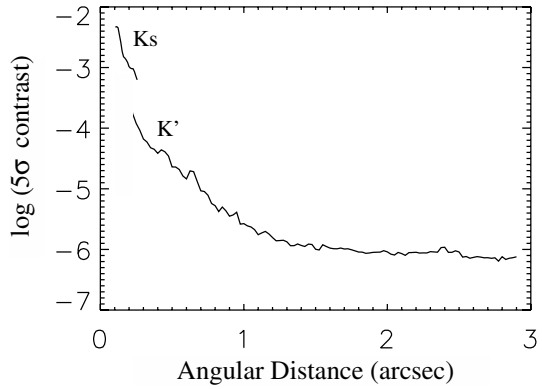

Figure 9. 5σ contrast limits for Jovian-mass bodies in or near the disk of MWC 758 derived from the K_s data (0.″1–0.″25), and the K' data ($r \geqslant 0.''25$). The discontinuity at 0.″25 reflects the change in exposure depth between the K_s and K' data sets.

and HD 142527 (Casassus et al. 2012; Rameau et al. 2012), the disk is dynamically warm ($h_c \geqslant 0.1$), indicating that spiral arms should be detectable in other warm disks, if Jovian-mass planets are present in the disk, and the region of the (sub)millimeter cavity retains at least some small-grain material. We identify potentially two arms in the disk of MWC 758, although we fit only the one with the larger angular coverage. The spiral arms are seen H, K' and K_s, and potentially also at 12 μm, demonstrating that they are visible both in scattered light and thermal emission. While unresolved, they are also detectable in *HST*/NICMOS 1.1 μm imagery. MWC 758 provides the first clear-cut case where an arm is optically thick, and shadows the outer disk, accounting for the disk non-detection with *HST*/STIS (IWA = 0.″5). The lack of similar shadowing of the west side of the disk suggests that the NW arm has a smaller amplitude, compatible with a lower mass.

Limitations of sparse-aperture masking in companion searches for Herbig Ae stars. Sparse-aperture masking trades contrast for resolution, realistically obtaining contrasts of 5–8 mag in the inner 0.″1. This is sufficient to detect brown dwarf and planetary companions to young, solar-like stars such as LkCa 15 and T Cha (Kraus & Ireland 2012; Huélamo et al. 2011). However, at ages >3 Myr, contrasts of >10 mag are required to detect exoplanet and low-mass (<30 M_J) brown dwarf companions to young, intermediate-mass stars such as MWC 758. Nonetheless, a close-in brown dwarf or stellar companion can have a significant impact on disk properties (see, e.g., Biller et al. 2012). Thus, constraining the existence of such a companion is key for realistic disk modeling of the full system.

Comparison of mass and luminosity constraints. Our mass estimate for the perturber of the SE arm is consistent with the presence of at least one Jovian-mass, but sub-brown dwarf mass planet in this system. The width of the submillimeter cavity and the dip in the IR SED are consistent with dynamical clearing by more than one body (Zhu et al. 2011), as is the presence of an inner disk with an inclination which is 20° larger than for the outer disk (Isella et al. 2008, 2010). The spiral arm appears to continue in to 0.″1, based on the K_s imagery, but characterizing the spiral requires imagery with higher Strehl ratio and smaller inner working angle than the data presented in this study. We estimate the mass of the SE arm perturber, based on surface brightness contrast, for the SE spiral to be 5^{+3}_{-4} M_J, consistent with the pattern being launched by a Jovian-mass planet and excluding a stellar or brown dwarf-mass perturber, independent of whether the perturber is in the disk or exterior to it. This is broadly consistent with the SAM constraints excluding a stellar mass companion within 0.″3 of the star, and ADI contrasts excluding brown dwarf mass bodies in the outer disk. Our 5σ contrast limit for an external companion is consistent with our perturber mass estimate, but does not inform on whether the perturber is has a luminosity compatible with the COND models, or is under-luminous relative to those models, as predicted for cold-start models of giant planets Spiegel & Burrows (2012). Higher contrast imagery will be required to constrain the luminosity evolution of any planetary-mass bodies in the disk of MWC 758.

Comparison with SAO 206462. MWC 758 resembles SAO 206462 in hosting two spiral arms that are trailing with respect to the disk rotation, and which are broadly consistent with being associated with Jovian-mass perturbing bodies. If the spiral arms

are independent patterns and are associated with giant planets, the presence of two arms each in SAO 206462 and MWC 758 and at least four in HD 142527 supports predictions that wide gaps must be cleared by multiple planets (Zhu et al. 2011). Our fit to the SE spiral arm suggests a perturber mass $\sim 10\times$ larger than for the SAO 206462 perturbers, consistent with shadowing of part of the outer disk. If sufficiently many transitional disks with spiral arms can be imaged, it will ultimately be possible to compare the giant planet mass function with studies of radial velocity giant planets, and to search for differences in the mass function as a function of stellar properties or system age.

Even at this early stage in the search for giant planets in transitional disks, the presence of spiral arms in systems with ages ranging from 3.7–5 Myr (MWC 758) to 9 ± 2 Myr (Müller et al. 2011, SAO206462) but otherwise similar levels of large grain depletion (Andrews et al. 2011) places constraints on whether there is a characteristic age for giant planet formation and disk clearing. In particular, our data can be reconciled with theoretical predictions that once gaps are opened, the inner disk should rapidly drain onto the star (Ercolano & Koepferl 2012), if and only if giant planet formation is a process with either a variable onset and/or duration.

A Planet and Inner Hole Formation. If the observed spiral structure is attributed to the existence of an unseen planet, such a planet might not account for the opening of the inner hole, since the location of the launching point is favored to be outside the location of the spirals (or the disk). Another possibility is that a planet that excites the spiral structures might actually be scattered from the inner disk, where the giant planet formation timescale is more rapid. In this case, the spiral fitting presented in this paper is relevant if the planet's eccentricity and inclination are well damped. If it still retains significant eccentricity, the shape of the spiral is more complicated and also there is a strong time variability within one orbit of the planet (Cresswell et al. 2007; Bitsch & Kley 2010). In this case, the fitting model for the spiral should be modified. We also note, that a planet external to the disk, if confirmed and found to be on an orbit indicating scattering from the inner disk, would imply that the disk of MWC 758 *must* host additional giant planets.

Implications for the future. MWC 758 has a steadily increasing body of data that indicates that the disk of this Herbig Ae star hosts at least two giant planets that are dynamically sculpting the disk, both by clearing a wide partial gap in the disk, and by exciting spiral density waves which can be traced in our data to 100–140 AU (depending on $d = 200$ or 279 pc) from the star. Such waves are expected to provide a means of funneling disk material onto and past any planets, until it reaches the star (Dodson-Robinson & Salyk 2011), consistent with both theoretical predictions for the point at which a companion can choke off accretion onto the star (Rice et al. 2006; Lubow & D'Angelo 2006) and the presence of on-going accretion onto the star (Beskrovnaya et al. 1999).

Higher Strehl ratio/angular resolution imagery are required to map the NW spiral in this system. Deeper ADI observations are also needed to either directly detect planets or to place more stringent luminosity limits on them. Such advances should be possible as the next generation of AO systems and coronagraphs commission in the course of the next year. Further advances are expected in the submillimeter: A key assumption made in this study is that the surface brightness contrast of the spiral arms is a reliable proxy for density contrast measurements made at wavelengths where the dust disk is optically thin. Such data with sufficient resolution to separate the arms from the bulk disk are required, and can be obtained once ALMA reaches its full capabilities, in late 2013.

This work, in part, is based on observations made with the NASA/ESA *Hubble Space Telescope*, obtained at the Space Telescope Science Institute, which is operated by the Association of Universities for Research in Astronomy, Inc., under NASA contract NAS 5-26555. The NICMOS observations are associated with program HST-GO-10177, while the STIS imagery is from HST-GTO-8474. The authors thank the support staff members of the IRTF telescope for assistance in obtaining the SED data, and the IR&D program at The Aerospace Corporation. This work is partially supported by KAKENHI 22000005 (M.T.), 23103002 (M.H. and M.H.), 23103004 (M.F.), and 24840037 (T.M.), WPI Initiative, MEXT, Japan (E.L.T.), NSF AST 1008440 (C.A.G.) and 1009203 (J.C.), and 1009314 (J.P.W.), and NASA NNH06CC28C (M.L.S.) and NNX09AC73G (C.A.G. and M.L.S.). T. C. was supported by a NASA Postdoctoral Fellowship for most of this work. We thank the anonymous referee for extremely helpful suggestions which have improved the paper.

REFERENCES

Andrews, S., Wilner, D. J., Espaillat, C., et al. 2011, ApJ, 732, 42
Baraffe, I., Chabrier, G., Allard, F., & Hauschildt, P. H. 1998, A&A, 337, 403
Baraffe, I., Chabrier, G., Allard, F., & Hauschildt, P. H. 2002, A&A, 382, 563
Baraffe, I., Charbrier, G., Barman, T. S., Allard, F., & Hauschilt, P. H. 2003, A&A, 402, 701
Beskrovnaya, N. G., Pogodin, M. A., Miroshnichenko, A. S., et al. 1999, A&A, 343, 163
Biller, B., Lacour, S., Juhász, A., et al. 2012, ApJ, 753, L38
Bitsch, B., & Kley, W. 2010, A&A, 523, A30
Bogaert, E. 1994, PhD thesis, Kathol. Univ.
Casassus, S., Perez, M. S., Jordán, A., et al. 2012, ApJL, 754, 31
Castillo-Rogez, J., Johnson, T. V., Lee, M. H., et al. 2009, Icarus, 204, 658
Chapillon, E., Guilloteau, S., Dutrey, A., & Piétu, V. 2008, A&A, 488, 565
Cresswell, P., Dirksen, G., Kley, W., & Nelson, R. P. 2007, A&A, 473, 329
Currie, T., Burrows, ., Itoh, Y., et al. 2011a, ApJ, 729, 128
Currie, T., Thalmann, C., Matsumura, S., et al. 2011b, ApJL, 736, 33
Currie, T., Burrows, A., Itoh, Y., et al. 2012, ApJL, 760, 32
D'Alessio, P., Calvet, N., Hartmann, L., Franco-Hernández, R., & Servín, H. 2006, ApJ, 638, 314
de Winter, D., van den Ancker, M. E., Maria, A., et al. 2001, A&A, 380, 609
Dodson-Robinson, S. E., & Salyk, C. 2011, ApJ, 738, 131
Dong, R., Rafikov, R., Zhu, Z., et al. 2012, ApJ, 750, 161
Dullemond, C. P., & Dominik, C. 2004, A&A, 421, 1075
Dullemond, C. P., & Dominik, C. 2005, A&A, 434, 971
Ercolano, B., & Koepferl, C. 2012, arXiv:1208.4689
Grady, C. A., Woodgate, B. E., Bowers, C. W., et al. 2005, ApJ, 630, 958
Hackwell, J. H., Warre, D. W., Chatelain, M. A., et al. 1990, Proc. SPIE, 1235, 171
Hashimoto, J., Tamura, M., Muto, T., et al. 2011, ApJ, 729, L17
Hodapp, K. W., Suzuki, R., Tamura, M., et al. 2008, Proc. SPIE, 7014, E42
Huélamo, N., Lacour, S., Tuthill, P., et al. 2011, A&A, 528, L7
Isella, A., Natta, A., Wilner, D., Carpenter, J. M., & Testi, L. 2010, ApJ, 725, 1735
Isella, A., Tatulli, E., Natta, A., & Testi, L. 2008, A&A, 483, L13
Juhász, A., Bouwman, J., Henning, Th., et al. 2010, ApJ, 721, 431
Kandori, R., Kusakabe, N., Tamura, M., et al. 2006, Proc. SPIE, 6269E, 159
Kim, S.-H., Martin, P. G., & Hendry, P. D. 1994, ApJ, 422, 164
Kraus, A., & Ireland, M. J. 2012, ApJ, 745, 5
Kusakabe, Nb., Grady, C. A., Sitko, M. L., et al. 2012, ApJ, 753, 153
Lacour, S., Tuthill, P., Amico, P., et al. 2011a, A&A, 532, A72
Lacour, S., Tuthill, P., Ireland, M., Amico, P., & Girard, J. 2011b, The Messenger, 146, 18
Lafreniére, D., Marois, C., Doyon, R., et al. 2007, ApJ, 660, 770
Lowrance, P. J., Becklin, E. E., Schneider, G., et al. 2005, AJ, 130, 1845
Lubow, S. H., & D'Angelo, G. 2006, ApJ, 641, 526
Malfait, K., Bogaert, E., & Waelkens, C. 1998, A&A, 331, 211
Mariñas, N., Telesco, C. M., Fisher, R. S., & Packham, C. 2011, ApJ, 737, 57

Marois, C., Lafreniére, D., Doyon, R., Macintosh, B., & Nadeau, D. 2006, ApJ, 641, 556
Martinache, F., Guyon, O., Clergeon, C., & Blain, C. 2012, Proc. SPIE, 8447, E1YM
Martinache, F., Guyon, O., Garrel, V., et al. 2011, Proc. SPIE, 8151E, 22
Martin-Zaïdi, C., Deleuil, M., Le Bourlot, J., et al. 2008, A&A, 484, 225
Meeus, G., Montesinos, B., Mendigutía, I., et al. 2012, A&A, 544, A78
Minowa, Y., Hayano, Y., Oya, S., et al. 2010, Proc. SPIE, 7736, E122
Müller, A., van den Ancker, M. E., Launhardt, R., et al. 2011, A&A, 530, A85
Muto, T., Grady, C. A., Hashimoto, J., et al. 2012, ApJ, 748, L22
Pereyra, A., Girart, J. M., Magalhães, A. M., Rodriques, C. V., & de Araújo, F. X. 2009, A&A, 501, 595
Rameau, J., Chauvin, G., Lagrange, A.-M., et al. 2012, A&A, 546, 24
Rice, W. K. M., Armitage, P. J., Wood, K., & Lodato, G. 2006, MNRAS, 373, 1619
Salyk, C., Blake, G. A., Boogert, A. C. A., & Brown, J. M. 2011, ApJ, 743, 112
Schneider, G., Silverstone, M. D., Hines, D. C., et al. 2006, ApJ, 650, 414
Spiegel, D., & Burrows, A. 2012, ApJ, 745, 174
Suzuki, R., Kudo, T., Hashimoto, J., et al. 2010, Proc. SPIE, 7735, E101
Tamura, M. 2009, in AIP Conf. Proc. 1158, Exoplanets and Disks: Their Formation and Diversity, ed. T. Usuda, M. Tamura, & M. Ishii (Melville, NY: AIP), 11
Tamura, M., Hodapp, K., Takami, H., et al. 2006, Proc. SPIE, 6269, E28
Thalmann, C., Grady, C. A., Goto, M., et al. 2010, ApJ, 718, L87
Tokunaga, A., Kobayashi, N., Bell, J., et al. 1998, Proc. SPIE, 3354, 512
Tuthill, P., Lacour, S., Amico, P., et al. 2010, Proc. SPIE, 7735, 56
Tuthill, P., Lloyd, J., Ireland, M., et al. 2006, Proc. SPIE, 6272, 56
van den Ancker, M. E., de Winter, D., & Tjin a Djie, H. R. E. 1998, A&A, 330, 145V
van Leeuwen, F. 2007, A&A, 474, 653
Whitney, B. A., Wood, K., Bjorkman, J. E., & Cohen, M. 2003a, ApJ, 598, 1079
Whitney, B. A., Wood, K., Bjorkman, J. E., & Wolff, M. J. 2003b, ApJ, 591, 1049
Wood, K., Wolff, M. J., Bjorkman, J. E., & Whitney, B. 2002, ApJ, 564, 887
Zhu, Z., Nelson, R. P., Dong, R., Espaillat, C., & Hartmann, L. 2012, ApJ, 755, 6
Zhu, Z., Nelson, R. P., Hartmann, L., Espaillat, C., & Calvet, N. 2011, ApJ, 729, 47